

Dalton Transactions

Accepted Manuscript



This is an *Accepted Manuscript*, which has been through the Royal Society of Chemistry peer review process and has been accepted for publication.

Accepted Manuscripts are published online shortly after acceptance, before technical editing, formatting and proof reading. Using this free service, authors can make their results available to the community, in citable form, before we publish the edited article. We will replace this *Accepted Manuscript* with the edited and formatted *Advance Article* as soon as it is available.

You can find more information about *Accepted Manuscripts* in the [Information for Authors](#).

Please note that technical editing may introduce minor changes to the text and/or graphics, which may alter content. The journal's standard [Terms & Conditions](#) and the [Ethical guidelines](#) still apply. In no event shall the Royal Society of Chemistry be held responsible for any errors or omissions in this *Accepted Manuscript* or any consequences arising from the use of any information it contains.

ARTICLE

Strong Steric Hindrance Effect on Ground State, Excited State, and Charge Separated State Properties of a Cu^I-Diimine Complex Captured by X-ray Transient Absorption Spectroscopy

Cite this: DOI: 10.1039/x0xx00000x

Received 00th January 2012,

Accepted 00th January 2012

DOI: 10.1039/x0xx00000x

www.rsc.org/

J. Huang^a, M. W. Mara^{a,b}, A. B. Stickrath^a, O. Kokhan^a, M. R. Harpham^a, M. K. Haldrup,^c M. L. Shelby^b, X. Zhang^d, R. Ruppert^e, J.-P. Sauvage^f, L. X. Chen^{a,b*}

Photophysical and structural properties of a Cu^I diimine complexes with very strong steric hindrance, [Cu^I(dppS)₂]⁺ (dppS=2,9-diphenyl-1,10-phenanthroline disulfonic acid disodium salt), are investigated using optical and X-ray transient absorption (OTA and XTA) spectroscopies. The bulky phenylsulfonic acid groups at 2, 9 positions of phenanthroline ligands force the ground state and the metal-to-ligand-charge-transfer (MLCT) excited state to adapt a flattened pseudo-tetrahedral coordination geometry in which the solvent access to the copper center is completely blocked. We analyzed the MLCT state dynamics and structures as well as those of the charge separated state resulted from the interfacial electron injection from the MLCT state to TiO₂ nanoparticles (NPs). The OTA results show an absence of the sub-picosecond component previously assigned as the time constant for flattening, while the two observed time constants are assigned to a relatively slow intersystem crossing (ISC) rate (~13.8 ps) and a decay rate (100 ns) of the [Cu^I(dppS)₂]⁺ MLCT state in water. These results correlate well with the XTA studies that resolved a flattened tetrahedral Cu(I) coordination geometry in the ground state. Probing the ³MLCT state structure with XTA establishes that ³MLCT state has the same oxidation state as the copper center in [Cu^{II}(dppS)₂]⁺ and Cu-N distance is reduced by 0.06 Å compared to that of ground state, accompanied by a rotation of phenyl rings located at 2,9 positions of phenanthroline. Structural dynamics of the photoinduced charge transfer process in the [Cu^I(dppS)₂]⁺/TiO₂ hybrid is also investigated, which suggests a more restricted environment for the complex upon binding to TiO₂ NPs. Moreover, the Cu-N bond length of the oxidized state of [Cu^I(dppS)₂]⁺ after electron injection to TiO₂ NPs shortens by 0.05 Å compared to that in ground state. The interpretation of these observed structural changes associated with excited and charge separated states will be discussed. These results not only set an example of applying XTA in capturing the intermediate structure of metal complex/semiconductor NPs hybrid but also provide the guidance for designing efficient Cu^I diimine complexes with optimized structures for its application in solar-to-electricity conversion.

Introduction

Cu^I diimine complexes, with similar light absorption as those of quintessential ruthenium complexes, have attracted much attention because of their potential applications in solar energy conversion¹⁻⁵ chemical sensing^{6, 7} and molecular devices^{8, 9}. Although these complexes have been studied since decades ago, studies in the past a few years are focused at their functions aligned with those performed by Ru(II) polypyridyl complexes in solar energy conversion. Cu^I diimine complexes have strong potentials to replace less abundant

Ru(II) complexes used in solar energy conversion, because in addition to their similar photophysical properties of MLCT (metal-to-ligand-charge-transfer) state as that of Ru(II) complexes, Cu^I diimine complexes are more environmentally and economically viable.¹⁰⁻¹⁵ Furthermore, the MLCT state of Cu^I diimine complexes, due to its electron transfer from the copper center to the ligand, yields a 3d⁹ electronic configuration that is susceptible to the Jahn-Teller distortion to transform an pseudo-tetrahedral geometry with a D_{2d} symmetry to a flattened tetrahedral geometry with a D₂ symmetry. Such excited state structural movements have been

explored for functions of molecular machines.¹² Therefore, it is important to gain the detailed knowledge on structural and environmental controls of the excited state properties of the Cu^I diimine complexes before they are employed to different applications in solar energy conversion.

Perhaps the most interesting aspect of these complexes is that their structural and environmental dependent photophysical properties, such as the MLCT state lifetimes, intersystem crossing rates and luminescence quantum yields. Also, the MLCT state of such complexes undergoes a transformation in the coordination geometry due to the different preferences of the electronic configurations of 3d¹⁰ Cu(I) in the ground state and 3d⁹ Cu(II) in the MLCT state.¹⁶ As summarized in a recent review,¹⁷ the MLCT state properties of a series of Cu^I bis-phenanthroline based complexes can be altered via different steric hindrance exerted by the substituents at the 2, 9 positions of the phenanthroline ligands that can modulate the angle between the two phenanthroline ligand planes from 90°, such as in the complex with 2,9-di-tert-butyl-1,10-phenanthroline ligands with an orthogonal tetrahedral coordinating geometry, to ~68°, a “flattened” tetrahedral geometry, such as in less hindered species that are capable of undergoing the flattening.^{4, 8, 13, 17-24} It has been observed that when the two phenanthroline ligand planes are forced to be orthogonal, the intersystem crossing (ISC) from ¹MLCT to ³MLCT state occurs on a few picosecond time scale, while the same process takes 10 - 15 ps when the two ligand planes are not orthogonal,^{19, 23-25} i.e., a flattened tetrahedral geometry. According to the calculations by Siddique et al.,²⁴ the spin-orbit coupling coefficients are lower for the states stabilizing at a flattened coordinating geometry due to the changes in the symmetry from D_{2d} to D₂, resulting in a relatively slow ISC rate. In addition, the ³MLCT excited state lifetimes and emission quantum yields are also sensitive to the capability of an “exciplex” formation with a solvent molecule, no matter the solvent is considered as coordinating and non-coordinating with the copper center. It has been shown that the presence of bulky groups at 2, 9 positions can block solvent access to the Cu center to prevent the formation of an “exciplex”, lowering the energy gap between the MLCT and the ground states and accelerating the ground state recovery, and thus result in a longer MLCT lifetime and a higher emission quantum yield.^{14, 15, 18, 26-29} These studies suggest that the excited state dynamics of Cu^I diimine complexes could be controlled by the dihedral angle between the two phenanthroline ligand planes as well as the solvent accessibility to the Cu center.

Previously we have investigated the structural influence on the excited state dynamics in an extreme case of a completely locked tetrahedral coordinating geometry due to the sterically-bulky t-butyl groups in bis(2,9-di-tert-butyl-1,10-phenanthroline)copper(I), [Cu^I(dtbp)₂]⁺.¹⁹ We showed that [Cu^I(dtbp)₂]⁺ has three microsecond ³MLCT lifetime, no sub-picosecond component that was previously assigned as the Jahn-Teller distortion of flattening of the pseudo-tetrahedral coordination geometry and a few picosecond intersystem crossing time constant. Because sufficient lifetimes and energetics are prerequisites for many photochemical processes as well as the sensitivity of these Cu^I excited state to their structures, we want to investigate whether the ¹MLCT and ³MLCT states lifetimes can be simultaneously prolonged in the Cu^I phenanthroline complexes with locked flattened geometry in both the ground and excited states. Furthermore, if these excited state lifetimes are extended through structural tuning, we may achieve sufficient efficiency of interfacial charge injection from these complexes to semiconductor nanoparticles in the dye-sensitized solar cells.^{2, 17, 25}

In this report, we examine the structural influence on the excited state dynamics of [Cu^I(dppS)₂]⁺ (dppS=2,9-diphenyl-1,10-phenanthroline disulfonic acid disodium salt) which represents another extreme that the complex is almost locked into flattened coordination geometry. In our recent paper,²⁵ we have reported an efficient electron injection process directly from ¹MLCT state of [Cu^I(dppS)₂]⁺ to TiO₂ NPs followed by ultraslow back electron transfer process. This observation has been attributed to the already flattened ground state geometry of [Cu^I(dppS)₂]⁺, which prolongs the ISC time to enable ET from the ¹MLCT state. While the successful electron injection has been studied in great detail, the quantitative structural analysis of the MLCT state as well as charge separated state in this Cu(I) diimine complex have not been reported. Here, our investigation is focused on detailed structural dynamics of these transient states of [Cu^I(dppS)₂]⁺ complex in excited state in H₂O and charge separated state formed after electron injection to TiO₂ NPs as well as their correlation with ground state structure. Optical transient absorption (TA) spectroscopy is used to determine excited MLCT state kinetics by monitoring the MLCT excited state absorption of [Cu^I(dppS)₂]⁺ in visible region. Analogous method in the X-ray regime, X-ray transient absorption (XTA) spectroscopy, is used to track electron configurations and corresponding molecular structural changes of [Cu^I(dppS)₂]⁺ by measuring transient X-ray absorption near edge structure (XANES) and extended X-ray absorption fine structure (EXAFS).^{17, 19, 22, 23, 25, 30-34} We would like to answer the following questions: (1) what are structures of the MLCT state and charge separate state structures; (2) what are the structural changes

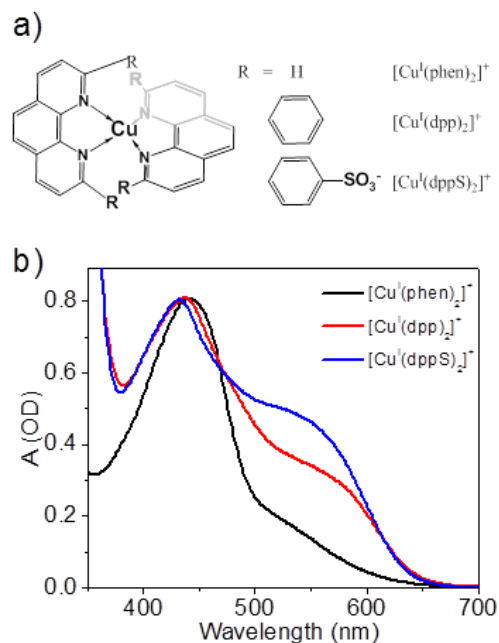


Figure 1. a) Molecular structures of [Cu^I(phen)₂]⁺, [Cu^I(dpp)₂]⁺, and [Cu^I(dppS)₂]⁺. b) UV-vis absorption spectra of [Cu^I(phen)₂]⁺ in dichloromethane (black), [Cu^I(dpp)₂]⁺ in dichloromethane (red), [Cu^I(dppS)₂]⁺ in water (blue).

of the complex when it binds to TiO₂ nanoparticles; and (3) what we can learn from our study on Cu^I diimine complex design for its applications in solar energy conversion? Understanding the molecular structures and dynamics of both photoexcited states and charge separated intermediates in the current system will not only provide the guidance of revealing their practical applications in dye

sensitized solar cells but also the insight into the nature of photochemical reactions.

Results and discussion

Ground State Photophysical Properties of $[\text{Cu}^{\text{I}}(\text{dppS})_2]^+$ in H_2O

UV-vis absorption spectrum of $[\text{Cu}^{\text{I}}(\text{dppS})_2]^+$ in H_2O (blue) is presented in Figure 1b. The spectra of $[\text{Cu}^{\text{I}}(\text{phen})_2]^+$ (black) and $[\text{Cu}^{\text{I}}(\text{dpp})_2]^+$ (red) in dichloromethane are also listed in Figure 1b for comparison. Analogous to those of $[\text{Cu}^{\text{I}}(\text{phen})_2]^+$ and $[\text{Cu}^{\text{I}}(\text{dpp})_2]^+$, the spectrum of $[\text{Cu}^{\text{I}}(\text{dppS})_2]^+$ is typically characterized by an intense main absorption peak at 420–470 nm region and a shoulder feature at lower energy, both of which have been assigned to MLCT bands based on previous studies^{17, 19, 22, 25, 34, 35} with the latter assigned as the MLCT transition from the flattened coordination geometry. Apparently, with the increasing steric hindrance at the 2, 9 positions of phenanthroline groups, i.e. $[\text{Cu}^{\text{I}}(\text{phen})_2]^+ > [\text{Cu}^{\text{I}}(\text{dpp})_2]^+ > [\text{Cu}^{\text{I}}(\text{dppS})_2]^+$ (Fig. 1a), the maximum position of the main absorption peak shifts to blue accompanied with the increasing relative intensity of the low-energy shoulder to the main absorption peak, indicating the correlation between the steric hindrance and the MLCT transitions. According to the DFT calculations by Siddeque et al.,²⁴ both excitation energies and oscillator strengths of MLCT transitions in Cu^{I} phenanthroline complexes, corresponding to the transitions between the $\text{Cu } 3d_{xz}$ and $3d_{yz}$ HOMOs and LUMOs orbitals, are strongly dependent on the dihedral angles of the two phenanthroline planes. When the dihedral angle of the two phenanthroline planes is 90° , the two transitions energies are nearly degenerate, therefore only the main peak in 440–460 nm region is expected in the absorption spectrum, which is represented by the extreme case of $[\text{Cu}^{\text{I}}(\text{dtbp})_2]^+$ as observed in our previous studies.³⁴ When the dihedral angle deviates from 90° through a flattening distortion from D_{2d} to D_2 , the two MLCT transition energies split, leading to a red-shift of the low-energy shoulder and a blue shift of the main MLCT absorption band. This is clearly seen in Figure 1a, where the main absorption band shows a blue shift and the shoulder shows a red shift in the most sterically hindered $[\text{Cu}^{\text{I}}(\text{dppS})_2]^+$. As shown here as well as our previous study,³⁴ the relative intensity of the low-energy shoulder measures the degree of dynamic flattening distortion in the ground state likely through low frequency rocking modes of the pseudo-tetrahedral coordination geometry in a D_{2d} symmetry,³⁵ with an increased shoulder intensity correlated to a larger flattening distortion. Therefore, the highest relative intensity shoulders in the spectrum of $[\text{Cu}^{\text{I}}(\text{dppS})_2]^+$ compared to those of $[\text{Cu}^{\text{I}}(\text{phen})_2]^+$ and $[\text{Cu}^{\text{I}}(\text{dpp})_2]^+$ suggested the largest degree of the flattening as well as other accompanying distortions. These results all support that $[\text{Cu}^{\text{I}}(\text{dppS})_2]^+$ with bulky groups at 2, 9 positions of the phenanthroline groups adapts a likely flattened geometry in the ground state, which is verified by our XANES results to be discussed later.

Excited State Dynamics of $[\text{Cu}^{\text{I}}(\text{dppS})_2]^+$ Complex in H_2O

Figure 2a shows the femtosecond transient absorption (fs-TA) spectra of $[\text{Cu}^{\text{I}}(\text{dppS})_2]^+$ complex in H_2O in visible region after 415 nm excitation. The entire spectra exhibit a broad positive absorption, and can be assigned to the MLCT state absorption. The spectral evolution for $[\text{Cu}^{\text{I}}(\text{dppS})_2]^+$ in H_2O were dominated by ISC from $^1\text{MLCT}$ to $^3\text{MLCT}$ state at early time (< 25 ps) and intrinsic $^3\text{MLCT}$ state decay at later time (> 25 ps). Figure 2b shows the kinetics trace of $[\text{Cu}^{\text{I}}(\text{dppS})_2]^+$ complex in H_2O at 570 nm. The kinetic trace fits a dual-exponential function which reveals two decay time constants,

$\tau_1 = 13.8$ ps and $\tau_2 \gg 3$ ns. τ_1 is consistent with the ISC time constant previously observed in $[\text{Cu}^{\text{I}}(\text{dpp})_2]^+$ (dpp=2,9-diphenyl-1,10-phenanthroline)³⁶ and in $[\text{Cu}^{\text{I}}(\text{dmp})_2]^+$ (dmp=2,9-dimethyl-1,10-phenanthroline) after the excited state flattening distortion,^{20, 21, 23, 24} and thus can be attributed to the ISC from $^1\text{MLCT}$ to $^3\text{MLCT}$ excited state. Compared to $[\text{Cu}^{\text{I}}(\text{dtbp})_2]^+$ with two phenanthroline ligand planes locked to orthogonal orientation with each other, ISC rate in

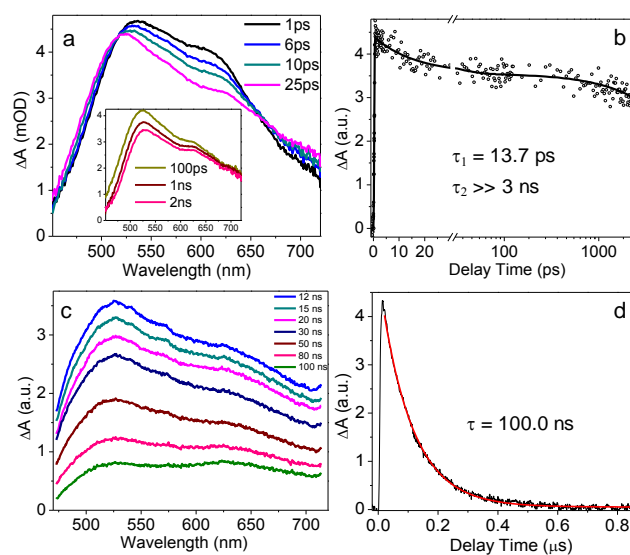


Figure 2. Femtosecond (a) and nanosecond (c) absorption spectra of $[\text{Cu}^{\text{I}}(\text{dppS})_2]^+$ in H_2O . Excited state kinetics trace of $[\text{Cu}^{\text{I}}(\text{dppS})_2]^+$ in H_2O at 570 nm measured by femtosecond (b) and nanosecond (d) absorption spectroscopy.

$[\text{Cu}^{\text{I}}(\text{dppS})_2]^+$ complex is several times slower. Meanwhile, this complex does not have a sub-ps component in its TA kinetics corresponding to the flattening as in $[\text{Cu}^{\text{I}}(\text{dmp})_2]^+$ ^{20, 21, 23} and structural reorganization as in $[\text{Cu}^{\text{I}}(\text{dpp})_2]^+$,²² indicating its severe steric hindrance prevents the Jahn-Teller distortion in the excited state, which will be further discussed in the XTA results. As discussed in previous studies, the prolonged ISC time constant is likely an indication of a flattened tetrahedral coordination geometry for the $\text{Cu}(\text{I})$ center in the ground state due to the strong steric hindrance of the two sulfonated phenyl ligands at 2, 9 positions of phenanthroline. Consequently, the spin-orbit coupling is significantly weakened and hence results in a slower ISC process and a prolonged $^1\text{MLCT}$ lifetime of 13.8 ps. The long decay time constant ($\gg 3$ ns) can be accurately determined by nanosecond absorption measurement (ns-TA) and assigned to the $^3\text{MLCT}$ state lifetime. The ns-TA spectra of $[\text{Cu}^{\text{I}}(\text{dppS})_2]^+$ complex in H_2O after 420 nm excitation (Figure 2c) show the dominating excited state absorption in the whole spectral window, similar to the results in the fs-TA measurement (Figure 2a). The kinetics monitored at the probe wavelengths 570 nm (Figure 2d) yields the $^3\text{MLCT}$ lifetime of ~ 100 ns, similar to that of $[\text{Cu}^{\text{I}}(\text{dpp})_2]^+$ in ethanol or acetonitrile.²³ In contrast, the $^3\text{MLCT}$ lifetime of $[\text{Cu}^{\text{I}}(\text{phen})_2]^+$ is only a few picosecond even in non-coordination solvent, dichloromethane,³⁴ and that of $[\text{Cu}^{\text{I}}(\text{dmp})_2]^+$, < 2 ns in coordination solvents.²³ Therefore, the prolonged $^3\text{MLCT}$ lifetime of $[\text{Cu}^{\text{I}}(\text{dppS})_2]^+$ suggests a complete shielding of the Cu center from the solvent, preventing the formation of an “exciplex” with the coordination solvent molecules. As mentioned earlier, the sub-ps rising component attributed to the excited state flattening dynamics in other Cu^{I} complexes,^{20, 23} was not observed in this system. These observations

further support the assignment that the ground state of $[\text{Cu}^{\text{I}}(\text{dppS})_2]^+$ complex is already locked in a “flattened” geometry, and hence no further flattening in the excited state. These results together indicate that $^1\text{MLCT}$ excited state of $[\text{Cu}^{\text{I}}(\text{dppS})_2]^+$ complex formed after excitation converts to $^3\text{MLCT}$ excited state without undergoing Jahn-Teller distortion, followed by $^3\text{MLCT}$ state decay with a 100-ns time constant.

Structural Dynamics of $[\text{Cu}^{\text{I}}(\text{dppS})_2]^+$ Complex in H_2O .

X-ray absorption spectroscopy (XAS) was used to directly extract the structures of $[\text{Cu}^{\text{I}}(\text{dppS})_2]^+$ in H_2O for the ground and excited states as shown in Figure 3. The Cu K-edge XANES (X-ray absorption near edge structure) spectrum for the ground state of $[\text{Cu}^{\text{I}}(\text{dppS})_2]^+$ (black plot, Fig. 3a) taken before the laser pulse arrives shows a rather pronounced peak in the middle of the transition edge attributed to the $1s \rightarrow 4p_z$ transition at 8.986 keV as assigned for the first row transition metal coordination environments from comprehensive studies of different model complexes,³⁷ and has been used to directly probe the dihedral angle of the two phenanthroline ligand planes of the Cu^{I} complex in the solution.³⁷ Such a capability is enabled by both experimental and theoretical studies showing that the intensity of $1s \rightarrow 4p_z$ edge features vary significantly for different Cu^{I} complexes with various coordination geometry.³⁷ The $1s \rightarrow 4p_z$ peak intensity is associated with the vacancy of the $4p_z$ orbital of the first row transition metal complexes, which changes with the coordination geometry. Hence, the more prominent $1s \rightarrow 4p_z$ peak intensity observed in $[\text{Cu}^{\text{I}}(\text{dppS})_2]^+$ than that of $[\text{Cu}^{\text{I}}(\text{phen})_2]^+$ complex³⁴ suggest more “flattened” tetrahedral coordination geometry for the copper center in the ground state, which is consistent with the MLCT transition analysis based on its UV-visible absorption spectrum.

X-ray transient absorption (XTA) spectroscopy^{32, 38-42} is used to study the excited state structural dynamics of $[\text{Cu}^{\text{I}}(\text{dppS})_2]^+$ in H_2O . The XANES spectrum of $[\text{Cu}^{\text{I}}(\text{dppS})_2]^+$ in H_2O with laser excitation is shown in Figure 3a (red plot). The laser-on spectrum is taken at 150 ps after the laser pump pulse, corresponding to the $^3\text{MLCT}$ state. Due to the presence of both ground state and excited state molecules in the system, the laser-on XANES spectrum represents an algebraic sum of both the MLCT excited and ground states at 150 ps time delay between the laser pump and the X-ray probe pulses. Therefore, the MLCT state XANES spectrum needs to be extracted by subtracting the contribution of the remaining ground state from the total spectrum. Based on the energy distinction of the shoulder feature for Cu^{I} species at 8.986 keV, the excited state spectrum (blue curve) was obtained by subtracting 55% of ground state from the laser-on spectrum until the shoulder feature at 8.986 keV disappears.

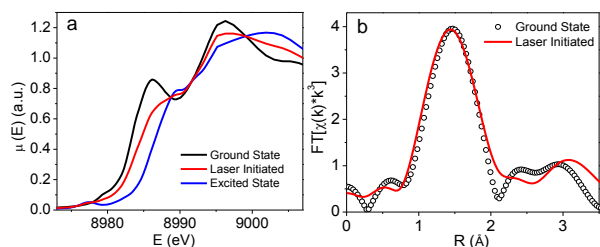


Figure 3. The XANES (a) and Fourier-transformed XAFS (b) spectra of $[\text{Cu}^{\text{I}}(\text{dppS})_2]^+$ in H_2O . The laser initiated spectrum (red) is collected at 150 ps after laser excitation. The blue curve in (a) is the spectrum of excited state for $[\text{Cu}^{\text{I}}(\text{dppS})_2]^+$ extracted from the laser initiated spectrum.

Similar to the previous studies on Cu^{I} diimine complexes,^{17, 22, 25, 30, 31, 34} the following spectral changes in the MLCT state compared to that of the ground state were observed: (1) the transition edge energy shifts to 3 eV higher, suggesting the higher positive charges in the copper center; (2) the shoulder feature at 8.986 keV, representing a $1s$ -to- $4p_z$ transition disappears, typically observed for transformation from Cu^{I} to Cu^{II} ; (3) a pre-edge feature at 8.979 keV appears which is attributed to a $1s$ - $3d$ transition that was only present for the Cu^{II} (d^9). These results for the ground and MLCT states for $[\text{Cu}^{\text{I}}(\text{dppS})_2]^+$ complex agree well with previously reported spectra for Cu diimine complexes and suggest a $\text{Cu}(\text{II})$ center in the MLCT state.

Figure 3b compares the XAFS spectra in R-space after Fourier transformation for the ground state (black open dot) and laser illuminated $[\text{Cu}^{\text{I}}(\text{dppS})_2]^+$ (red solid plot). The Fourier transforms of these XAFS spectra were processed within the k -range of 2.6 - 7.6 \AA^{-1} with a k^3 weighting. The peaks in these spectra present a radial distribution of Cu-neighboring atom distances in the complex without the phase corrections. The first peak, the Cu-N scattering paths, shifts to a smaller R for the laser illuminated $[\text{Cu}^{\text{I}}(\text{dppS})_2]^+$ compared to that in the ground state, suggesting the decrease of the average Cu-N distance in the laser illuminated sample. Furthermore, the magnitudes as well as the peak positions at R -range of 2 - 3.5 \AA for laser illuminated $[\text{Cu}^{\text{I}}(\text{dppS})_2]^+$ reveal difference from that of ground state $[\text{Cu}^{\text{I}}(\text{dppS})_2]^+$. The peaks at this region correspond to the Cu-C distances associated with C atoms of the phenanthroline connected directly to the four Cu-ligating N atoms as well as the C atoms of the phenyl groups in the 2,9 positions of phenanthroline.

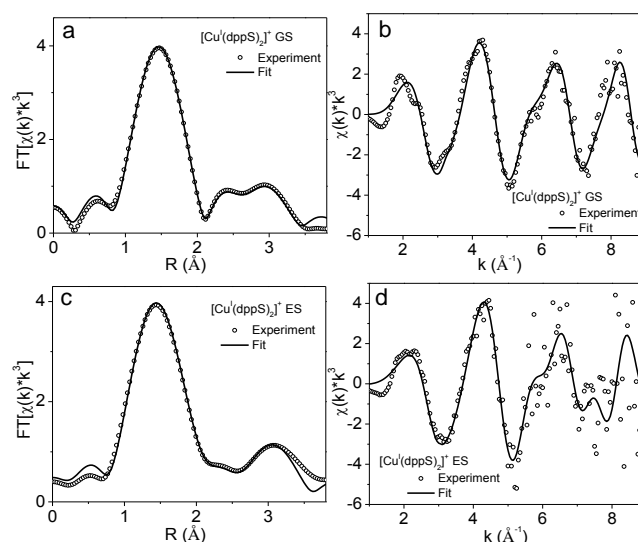


Figure 4. XAFS spectra (open dot) and the best fit (solid line) of $[\text{Cu}^{\text{I}}(\text{dppS})_2]^+$ in H_2O : (a) R-space, ground state, (b) k-space, ground state, (c) R-space, excited state, (d) k-space, excited state.

The change of these Cu-ligands can be quantified by fitting the experimental data using IFEFFIT program.

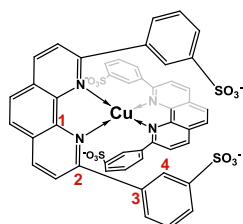
Figure 4 displays the fits to the XAFS spectra in both R- and k-space for GS and excited state of $[\text{Cu}^{\text{I}}(\text{dppS})_2]^+$, respectively. The results of data analysis for the nearest-neighboring shell from Cu ion are listed in Table 1. For the laser illuminated sample, the spectrum is fitted using a two bond length model, in which the average Cu-ligand bond distance is fit to two

Table I. XAFS Fitting Parameters^a of [Cu^I(dppS)₂]⁺ in H₂O

Vector	N	R(Å)	σ ² (Å ²)
Cu-N (GS) ^b	4	2.00	0.009
(ES) ^c	4	1.94	0.006
Cu-C ₁ (GS)	4	2.68	0.002
(ES)	4	2.65	0.001
Cu-C ₂ (GS)	4	2.90	0.002
(ES)	4	2.85	0.010
Cu-C ₃ (GS)	4	3.18	0.001
(ES)	4	3.00	0.001
Cu-C ₄ (GS)	4	3.32	0.002
(ES)	4	3.25	0.001

^aThe fitting precision for distance is ±0.01 Å, and 0.5 for N, the coordination number; ^bGS: ground state. ^cES: excited state

distances with one distance fixed at its corresponding Cu-ligand distance obtained from ground state spectrum fitting with 55% fraction to account for the contribution of the ground state molecules to the laser illuminated spectrum. Using this approach, the laser illuminated spectrum can be adequately fit with an average Cu-N distance of 1.94 Å for [Cu^I(dppS)₂]⁺ in MLCT excited state, which is shortened by 0.06 Å relative to ground state [Cu^I(dppS)₂]⁺. In addition, the Cu-C₁ and Cu-C₂ bond distances (indicated in Scheme I) are 0.03 and 0.05 Å shorter, respectively, in the MLCT state than in the ground state. This distance change is expected because C₁ and C₂ atoms in the phenanthroline are directly connected to the four Cu-ligating N atoms. It is interesting to note that a larger shortening of Cu-C₃ bond distance 0.18 Å is observed, while Cu-C₄ bond distance reveals a relatively small change with 0.07 Å shorter than in ground



Scheme I. Atom centers used in XAFS data fitting

state. This change suggests that the larger change of Cu-C₃ bond distance compared to the Cu-C₄ distance may be due to the phenyl ring rotation, shortened by 0.06 Å relative to the ground state [Cu^I(dppS)₂]⁺.

In addition to the solution [Cu^I(dppS)₂]⁺ MLCT excited state structure, we also investigated the geometry change of the complex upon its attachment onto TiO₂ nanoparticles (NPs). Figure 5a compares the XANES spectra of [Cu^I(dppS)₂]⁺ in solution and on the

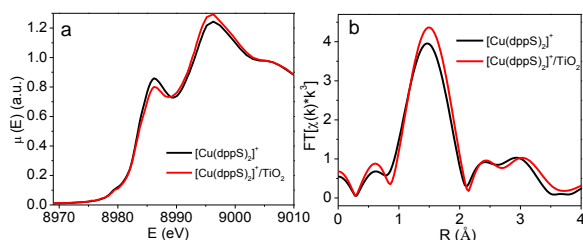


Figure 5. Comparison of the XANES (a) and the Fourier-transformed XAFS (b) spectra between [Cu^I(dppS)₂]⁺ in H₂O (black) and [Cu^I(dppS)₂]⁺/TiO₂ (red) in ground state.

TiO₂ nanoparticle surface. In both cases, the 1s-4p_z transition energy remains the same at 8.986 keV, while the intensity in the latter is lowered accompanied by a simultaneous increase of the whiteline intensity at 8.997 keV. Because the correlations between the 1s-4p_z transition intensity and the angle between the ligand planes has been established in comparing the intensity of this feature between the tetrahedral [Cu^I(dmp)₂]⁺ and flattened [Cu^I(dpp)₂]⁺ in our previous studies,³⁶ the reduced intensity can be attributed to a possible increase of the angle between the two phenanthroline ligand planes (or less flattened). It is known that the oxidation of Cu^I to Cu^{II} in [Cu^I(dppS)₂]⁺ is not only featured by the reduced 1s-4p_z transition, but also featured by the edge shift to higher energy, the emerging of 1s-3d pre-edge feature at 8.979 keV, as well as the reduced band at 8.996 keV. None of these additional features were observed in the XANES spectrum of [Cu^I(dppS)₂]⁺/TiO₂ hybrid, suggesting that the formation of [Cu^{II}(dppS)₂]²⁺ in [Cu^I(dppS)₂]⁺/TiO₂ hybrid can be excluded. These results indicate that a less flattened geometry of [Cu^I(dppS)₂]⁺ was observed in [Cu^I(dppS)₂]⁺/TiO₂ hybrid.

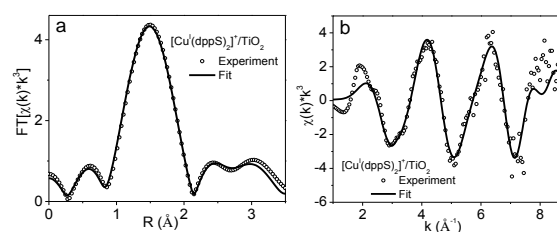


Figure 6. The best fits of XAFS spectra in R- (a) and k-space (b) for [Cu^I(dppS)₂]⁺/TiO₂ in ground state.

The comparison of the XAFS spectra of [Cu^I(dppS)₂]⁺ in H₂O and on TiO₂ NPs in R-space after Fourier transformation is presented in Figure 5b. Compared to [Cu^I(dppS)₂]⁺ in H₂O, the Cu-N peak for [Cu^I(dppS)₂]⁺/TiO₂ hybrid showed enhanced intensity. The increased peak amplitude, in general, can be attributed to an increase of the coordination number or a narrower conformation distribution due to restricted environments, i. e. smaller debye-waller factor. In this case, due to the two bulky sulfonated phenyl groups in the 2,9 positions of phenanthroline which blocks solvent access, it is unlikely that ligation can occur in the hybrid. Therefore, we attributed the increased Cu-N peak amplitude to the more restricted environment caused by binding to TiO₂ nanoparticles which further restricted the dynamic movement of the ligands. This result can be confirmed by comparing the debye-waller factor of Cu-N bond in [Cu^I(dppS)₂]⁺/TiO₂ hybrid sample with [Cu^I(dppS)₂]⁺. The best fits of XAFS spectra of [Cu^I(dppS)₂]⁺/TiO₂ at R and k-space are shown in Figure 6 and their fitting results are listed in Table II. A notable reduced debye-waller factor of Cu-N bond was observed in [Cu^I(dppS)₂]⁺/TiO₂ hybrid, which is consistent with the assignment of more restricted environment of [Cu^I(dppS)₂]⁺ after attaching to TiO₂ NPs. All of these results suggest that the complex adopted a less flattened geometry after linking to TiO₂ NPs.

Table II. XAFS Fitting Parameters^a of [Cu^I(dppS)₂]⁺/TiO₂

Vector	N	R(Å)	σ ² (Å ²)
Cu-N (GS)	4	1.99	0.006
(OS)	4	1.94	0.009
Cu-C ₁ (GS)	4	2.48	0.001
(OS)	4	2.44	0.007
Cu-C ₂ (GS)	4	2.74	0.005

(OS)	4	2.72	0.004
Cu-C ₃ (GS)	4	3.31	0.001
(OS)	4	3.47	0.010
Cu-C ₄ (GS)	4	3.55	0.002
(OS)	4	3.58	0.001

^oOS: oxidized state.

We have previously demonstrated efficient electron injection from the MLCT state of $[\text{Cu}^{\text{I}}(\text{dppS})_2]^+$ to TiO_2 nanoparticles using a combined EPR, TA, and XTA spectroscopy characterization.²⁵ Electron injection to TiO_2 NPs was unambiguously determined by probing the formation of the electron injection product, i.e. oxidized state $[\text{Cu}^{\text{II}}(\text{dppS})_2]^{+2}$, monitoring the XANES region of the spectrum collected at 9 ns when the MLCT state population in the hybrid can be neglected. In order to extract the intermediate structure of $[\text{Cu}^{\text{I}}(\text{dppS})_2]^+$ in $[\text{Cu}^{\text{I}}(\text{dppS})_2]^+/\text{TiO}_2$ hybrid associated with electron transfer process in the hybrid, here we analyzed its XAFS spectrum taken at 9 ns delay, which represents $[\text{Cu}^{\text{II}}(\text{dppS})_2]^{+2}$ as a result of the oxidized $[\text{Cu}^{\text{I}}(\text{dppS})_2]^+$ after the electron injection. The XAFS spectra for $[\text{Cu}^{\text{I}}(\text{dppS})_2]^+$ in $[\text{Cu}^{\text{I}}(\text{dppS})_2]^+/\text{TiO}_2$ hybrid at R- and k-space after Fourier transformation as well as their best fits are presented in Figure 7. The structural parameters for the distance from the copper center to neighboring shells from the XAFS analysis are also listed in Table II. Analogous to previous fitting approach, the laser initiated spectrum was fit using a two bond model with one distance fixed at the same parameters for ground state fitting. In this case, the fraction for ground state of $[\text{Cu}^{\text{I}}(\text{dppS})_2]^+$ is 75% to account for the contribution from the remaining ground state to the laser initiated spectrum. From the fitting results, we observed that Cu-N bond distance in oxidized state of $[\text{Cu}^{\text{I}}(\text{dppS})_2]^+$ in the hybrid is decreased by 0.05 Å compared to that in ground state. Similar to the results observed in $[\text{Cu}^{\text{I}}(\text{dppS})_2]^+$ in H_2O , Cu-C₁ and Cu-C₂ bond distance also decreases with Cu-N distance, which is expected because C₁ and C₂ are directly connected to the four Cu-ligating N atoms in the phenanthroline rings. In comparison to the MLCT state structure, the Cu-C₁ is much shorter in the oxidized intermediate $[\text{Cu}^{\text{II}}(\text{dppS})_2]^{+2}/\text{TiO}_2$ than that in the MLCT state in solution, which may reflect the electronic configuration difference in the two states.

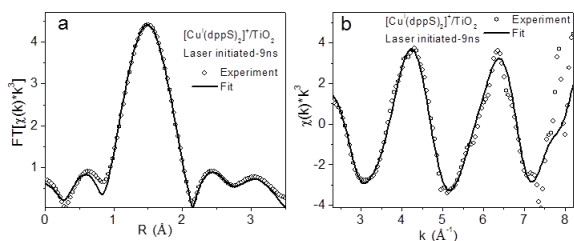


Figure 7. The best fits of XAFS spectra in R- (a) and k-space (b) for $[\text{Cu}^{\text{I}}(\text{dppS})_2]^+/\text{TiO}_2$ taken at 9 ns after laser excitation (75% ground state and 25% oxidized state).

In the oxidized intermediate, an electron is taken away by TiO_2 NP while the MLCT state merely shifts an electron to the ligand. Therefore, the oxidized intermediate has less electron density at the ligand, which may attribute to the overall shorter Cu-C₁ distances. Unlike the Cu-C₃ and Cu-C₄ bond distance decrease in the MLCT state of $[\text{Cu}^{\text{I}}(\text{dppS})_2]^+$ in H_2O from those of the ground state, Cu-C₃ distance is elongated significantly while Cu-C₄ bond distance increases slightly in the hybrid. These results suggest that after linking to TiO_2 NPs, $[\text{Cu}^{\text{I}}(\text{dppS})_2]^+$ has a more sterically restricted environment, which pushes the phenyl rings at 2,9 positions outbound accompanying the rotation of phenyl rings at 2,9 positions.

Experimental

Sample preparation.

$[\text{Cu}^{\text{I}}(\text{dppS})_2]^+\text{PF}_6^-$ was synthesized according to previously published procedures.²⁵ The concentration of $[\text{Cu}^{\text{I}}(\text{dppS})_2]^+\text{PF}_6^-$ used for the transient optical and X-ray absorption measurements was about 1 mM and used without degassing. TiO_2 nanoparticles (NPs) with average sizes 5-10 nm in diameter were purchased from Skyspring Nanomaterials, Inc. and used without further purification. $[\text{Cu}^{\text{I}}(\text{dppS})_2]^+\text{PF}_6^-$ sensitized TiO_2 NP suspension was prepared using the same approach as that in the recently published paper.²⁵

Femtosecond absorption spectroscopy.

The pump-probe transient absorption setup used for this study was based on an amplified Ti: sapphire laser system as described elsewhere.²⁵ Pump pulses at 415 nm were generated from the second harmonic of the 830 nm amplifier output of the regenerative amplifier. The pump beam at the sample had a diameter of 300 μm. The energy of the 415 nm pulse used for the measurement was controlled by variable neutral density filter wheel. The white light continuum probe were generated by focusing a few μJ of the Ti:sapphire amplifier output onto a sapphire window. The widths of the pump and probe pulses were about 150 fs, and the total instrumental response for the pump-probe experiments was about 180 fs. The sample cuvette path length was 2 mm. During the data collection, samples were constantly stirred to avoid photodegradation.

X-ray Transient absorption (XTA) spectroscopy.

The XTA measurements were carried out at 11ID-D, the Advanced Photon Source of Argonne National Laboratory as described previously. The laser pump pulse was the second harmonic output of a Nd:YLF regenerative amplified laser with 1 kHz repetition rate, giving 527 nm laser pulses with 5 ps fwhm. The X-ray probe pulses were derived from electron bunches extracted from the storage ring with 80 ps fwhm and 6.5 MHz repetition rate. The laser pump X-ray probe cycle was 1 kHz limited by the laser repetition rate. The laser and X-ray pulses intersect at a flowing sample stream of highly dispersed $[\text{Cu}^{\text{I}}(\text{dppS})_2]$ (BF4) (1 mM)-sensitized TiO_2 nanoparticles suspended in nanoporous H_2O with continuous purging of dry nitrogen gas and circulated using a peristaltic pump. The suspension of dye-attached TiO_2 nanoparticles forms a free jet of 550 μm in diameter. The delay between the laser and X-ray was adjusted by a programmable delay line (PDL-100A-20NS, Colby Instruments) that adjusted the phase shift of the mode-lock driver for the seed laser relative to that of the RF signal of the storage ring with a precision of 500 fs. The zero delay time by our definition is the peak of laser pulse and the peak of X-ray pulse coincident in timing space. Two photomultiplier tubes (PMTs) coupled to plastic scintillators were used at 90° angle on both sides to the incident X-ray beam to collect the X-ray fluorescence signals. A soller slit/Ni filter combination, which was custom-designed for the specific sample chamber configuration and for the distance between the sample and the detector, was inserted between the sample fluid jet and the PMT detectors. The current mode of the PMTs was used to acquire multiple photons from each X-ray pulse as the flux of the X-ray photons exceeded significantly the single photon counting limit. The outputs of the PMTs were sent to two fast analyzer cards (Agilent) that were triggered by a signal at 1 kHz from the scattered laser light collected by a photo diode. The card

digitized the X-ray fluorescence signals as a function of time at 1 ns/point after each trigger. The process was repeated and integrated for 4 s at each energy point. The signal intensity was the integrated area of the pulsed signal extracted by an in situ curve fitting procedure (G. Jennings, unpublished results). The fluorescence signals from the synchronized X-ray pulse at nominally 9 ns delay after the laser pump pulse excitation were collected to construct the spectrum for the oxidized state, and the fluorescence signals from the same X-ray pulse averaged over its 50 round trips in the storage ring prior to the laser pulse were averaged to construct the spectrum for the ground state.

Conclusions

Our structural and dynamics studies on $[\text{Cu}^{\text{I}}(\text{dppS})_2]^+$ complex in water and in a constraint $[\text{Cu}^{\text{I}}(\text{dppS})_2]^+/\text{TiO}_2$ hybrid studies revealed a flattened coordination geometry in both environments for the complex, which ensured a slower ISC rate that allows the interfacial electron injection to TiO_2 from a $^1\text{MLCT}$ state. The structural difference around the copper center at the interface with the TiO_2 nanoparticle from that in water suggested a highly constraint environment which causes distortion of the $[\text{Cu}^{\text{I}}(\text{dppS})_2]^+$ structure via binding. Also observed are the structural difference in the $^3\text{MLCT}$ state compared to the ground state with shortening of the Cu-N distance due to the stronger electrostatic interactions between the metal center and the ligand in solution. However, the structural change between the oxidized intermediate $[\text{Cu}^{\text{II}}(\text{dppS})_2]^{+2}/\text{TiO}_2$ and its ground state is significantly less due to the constraint the environment. The capability of obtaining structural details in environmental dependent photoinduced interfacial charge transfer system provides opportunities to theoretically model these systems to gain insight into the transient structural-functional correlation on the time scale of the charge separation, and the structural guidance in materials design.

Acknowledgements

We thank the support from the U. S. Department of Energy, Office of Science, Office of Basic Energy Sciences, under Contract No. DE-AC02-06CH11357. Use of the Advanced Photon Source at Argonne National Laboratory was supported by the U. S. Department of Energy, Office of Science, Office of Basic Energy Sciences, under Contract No. DE-AC02-06CH11357. The authors would like to thank Drs. Klaus Attenkofer (now at NSLS-II, Brookhaven National Laboratory), Guy Jennings, and Mr. Charles Kurtz of the Advanced Photon Source for their contributions to the Beamline 11ID-D facility at the APS. The instrumentation supports (to LXC et al.) from the US Department of Energy for purchasing lasers, detectors and other related equipment enabling the initiation and upgrade of XTA experiments at Beamline 11IDD are greatly appreciated.

Notes and references

^aChemical Sciences and Engineering Division, Argonne National Laboratory, Lemont, Illinois 60439, USA.

^bDepartment of Chemistry, Northwestern University, Evanston, Illinois, 60208, USA.

^cCentre for Molecular Movies, Department of Physics, NEXMAP Section, Technical University of Denmark, 2800 Kgs. Lyngby, Denmark.

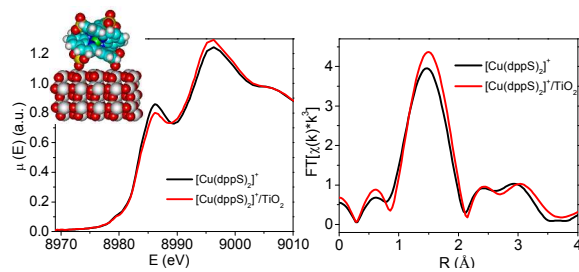
^dX-ray Science Division, Argonne National Laboratory, Lemont, IL 60439, USA.

^eInstitut de Science et d'Ingénierie Supramoléculaires and ^fInstitut de Chimie, Université de Strasbourg, 67000 Strasbourg, France.

1. N. Alonsovalente, J. F. Nierengarten and J. P. Sauvage, *J. Chem. Soc. Dalton Trans.*, 1994, 1649-1654.
2. T. Bessho, E. C. Constable, M. Gratzel, A. H. Redondo, C. E. Housecroft, W. Kylberg, M. K. Nazeeruddin, M. Neuburger and S. Schaffner, *Chem Commun*, 2008, 3717-3719.
3. J. K. McCusker, *Accounts Chem. Res.*, 2003, **36**, 876-887.
4. M. Ruthkosky, C. A. Kelly, M. C. Zaros and G. J. Meyer, *J. Am. Chem. Soc.*, 1997, **119**, 12004-12005.
5. S. K. Sakaki, T.; Hamada, T., *J. Chem. Soc. Dalton Trans.*, 2002, 840-842.
6. P. Thanasekaran, R.-T. Liao, Y.-H. Liu, T. Rajendran, S. Rajagopal and K.-L. Lu, *Coord. Chem. Rev.*, 2005, **249**, 1085-1110.
7. T. A. Vannelli and T. B. Karpishin, *Inorg Chem*, 2000, **39**, 1336-1336.
8. N. Armaroli, V. Balzani, F. Barigelletti, L. Decola, L. Flamigni, J. P. Sauvage and C. Hemmert, *J. Am. Chem. Soc.*, 1994, **116**, 5211-5217.
9. J.-P. Collin, C. Dietrich-Buchecker, P. Gavina, M. C. Jimenez-Molero and J.-P. Sauvage, *Accounts Chem. Res.*, 2001, **34**, 477-487.
10. N. Armaroli, *Chem. Soc. Rev.*, 2001, **30**, 113-124.
11. C. T. Cunningham, K. L. H. Cunningham, J. F. Michalec and D. R. McMillin, *Inorg Chem*, 1999, **38**, 4388-4392.
12. F. Durolo, J. Lux and J. Sauvage, *Chem. Eur. J.*, 2009, **15**, 4124-4134.
13. D. R. McMillin, J. R. Kirchoff and K. V. Goodwin, *Coord. Chem. Rev.*, 1985, **64**, 83-92.
14. M. T. Miller, P. K. Gantzel and T. B. Karpishin, *J. Am. Chem. Soc.*, 1999, **121**, 4292-4293.
15. D. V. Scaltrito, D. W. Thompson, J. A. O'Callaghan and G. J. Meyer, *Coord. Chem. Rev.*, 2000, **208**, 243-266.
16. D. R. McMillin and K. M. McNett, *Chemical Reviews*, 1998, **98**, 1201-1219.
17. M. W. Mara, K. A. Fransted and L. X. Chen, *Coord. Chem. Rev.*, 2014, **Online June 2014**.
18. M. K. Eggleston, D. R. McMillin, K. S. Koenig and A. J. Pallenberg, *Inorg Chem*, 1997, **36**, 172-176.
19. N. A. Gothard, M. W. Mara, J. Huang, J. M. Szarko, B. S. Rolczynski and L. X. Chen, *J. Phys. Chem. A.*, 2012, **116**, 1984-1992.
20. M. Iwamura, S. Takeuchi and T. Tahara, *J. Am. Chem. Soc.*, 2007, **129**, 5248-5256.
21. M. Iwamura, S. Takeuchi and T. Tahara, *Phys. Chem. Chem. Phys.*, 2014, **16**, 4143-4154.
22. M. W. Mara, N. E. Jackson, J. Huang, A. B. Stickrath, X. Y. Zhang, N. A. Gothard, M. A. Ratner and L. X. Chen, *J. Phys. Chem. B*, 2013, **117**, 1921-1931.
23. G. B. Shaw, C. D. Grant, H. Shirota, E. W. Castner, G. J. Meyer and L. X. Chen, *J. Am. Chem. Soc.*, 2007, **129**, 2147-2160.
24. Z. A. Siddique, Y. Yamamoto, T. Ohno and K. Nozaki, *Inorg Chem*, 2003, **42**, 6366-6378.
25. J. Huang, B. Onur, M. W. Mara, O. Buyukcakir, N. Coskun, N. M. Dimitrijevic, G. Barin, O. Kokhan, A. B. Stickrath, R. Ruppert,

- J. P. Sauvage, F. J. Stoddart and L. X. Chen, *Angew. Chem. Intl. Ed.*, 2012, **51**, 12711.
26. R. M. Everly, R. Ziessel, J. Suffert and D. R. McMillin, *Inorg Chem*, 1991, **30**, 559-561.
27. V. Kalsani, M. Schmittel, A. Listorti, G. Accorsi and N. Armaroli, *Inorg Chem*, 2006, **45**, 2061-2067.
28. M. T. Miller and T. B. Karpishin, *Inorg Chem*, 1999, **38**, 5246-5249.
29. M. T. Miller, P. K. Gantzel and T. B. Karpishin, *Inorg Chem*, 1999, **38**, 3414-3422.
30. L. X. Chen, G. Jennings, T. Liu, D. J. Gosztola, J. P. Hessler, D. V. Scaltrito and G. J. Meyer, *J. Am. Chem. Soc.*, 2002, **124**, 10861-10867.
31. L. X. Chen, G. B. Shaw, I. Novozhilova, T. Liu, G. Jennings, K. Attenkofer, G. J. Meyer and P. Coppens, *J. Am. Chem. Soc.*, 2003, **125**, 7022-7034.
32. L. X. Chen and X. Zhang, *J. Phys. Chem. Lett.*, 2013, **4**, 4000-4013
33. K. A. Fransted, N. E. Jackson, R. Zong, M. W. Mara, H. Huang, M. R. Harpham, M. L. Shelby, R. P. Thummel and L. X. Chen, *J. Phys. Chem. A.*, 2014, DOI: **10.1021/jp504294j**.
34. J. V. Lockard, S. Kabehie, G. Smolentsev, A. Soldatov, Z. J. I. and L. X. Chen, *J. Phys. Chem. B.*, 2010, **114**, 14521-14527.
35. M. Z. Zgierski, *J. Chem. Phys.*, 2003, **118**, 4045-4051.
36. M. W. Mara, N. E. Jackson, J. Huang, A. B. Stickrath, X. Zhang, N. A. Gothard, M. A. Ratner and L. X. Chen, *Journal of Physical Chemistry B*, 2013, **117**, 1921-1931.
37. L. S. Kau, D. J. Spirasolomon, J. E. Pennerhahn, K. O. Hodgson and E. I. Solomon, *J. Am. Chem. Soc.*, 1987, **109**, 6433-6442.
38. L. X. Chen, X. Zhang and M. L. Shelby, *Chem. Sci.*, 2014, DOI: 10.1039/C1034SC01333F.
39. L. X. Chen, *Ann. Rev. Phys. Chem.*, 2005, **56**, 221-254.
40. L. X. Chen, *Angew. Chemie, Intl. Ed.*, 2004, **43**, 2886-2905.
41. C. Bressler and M. Chergui, *Ann. Rev. Phys. Chem.*, 2010, **61**, 263-282.
42. C. Bressler and M. Chergui, *Chem. Rev.*, 2004, **104**, 1781-1812.

TOC figure:



TOC text:

Steady-state and transient structures of a copper diimine dye sensitizer on TiO₂ nanoparticles undergoing photoinduced interfacial electron transfer are determined.